

Fermionic response from fractionalization in an insulating two-dimensional magnet

J. Nasu^{1*}, J. Knolle^{2*}, D. L. Kovrizhin^{2,3}, Y. Motome⁴ and R. Moessner⁵

Conventionally ordered magnets possess bosonic elementary excitations, called magnons. By contrast, no magnetic insulators in more than one dimension are known whose excitations are not bosons but fermions. Theoretically, some quantum spin liquids (QSLs)¹—new topological phases that can occur when quantum fluctuations preclude an ordered state—are known to exhibit Majorana fermions² as quasiparticles arising from fractionalization of spins³. Alas, despite much searching, their experimental observation remains elusive. Here, we show that fermionic excitations are remarkably directly evident in experimental Raman scattering data⁴ across a broad energy and temperature range in the two-dimensional material α -RuCl₃. This shows the importance of magnetic materials as hosts of Majorana fermions. In turn, this first systematic evaluation of the dynamics of a QSL at finite temperature emphasizes the role of excited states for detecting such exotic properties associated with otherwise hard-to-identify topological QSLs.

The Kitaev model has recently attracted attention as a canonical example of a QSL with emergent fractionalized fermionic excitations^{2,5}. The model is defined for $S = 1/2$ spins on a honeycomb lattice with anisotropic bond-dependent interactions, as shown in Fig. 1a². Recent theoretical work—by providing access to properties of excited states—has predicted signs of Kitaev QSLs in the dynamical response at $T = 0$ (refs 6,7) and in the T dependence of thermodynamic quantities^{8,9}. However, the dynamical properties at finite T have remained a theoretical challenge, as it is necessary to handle quantum and thermal fluctuations simultaneously. Here, by calculating dynamical correlation functions over a wide temperature range, we directly identify signatures of fractionalization in available experimental inelastic light scattering data.

In real materials, Kitaev-type anisotropic interactions may appear through a superexchange process between $j_{\text{eff}} = 1/2$ localized moments in the presence of strong spin-orbit coupling¹⁰. Such a situation is believed to be realized in several materials, such as iridates A₂IrO₃ (A = Li, Na)^{11,12} and a ruthenium compound α -RuCl₃ (refs 4,13–15). These materials show magnetic ordering at a low T (~ 10 K), indicating that some exchange interactions coexist with the Kitaev exchange and give rise to the magnetic order instead of the QSL ground state^{16–19}. Nevertheless, evidence suggests that the Kitaev interaction is predominant (several tens to hundreds of kelvin)^{15,18–22}, which may provide an opportunity to observe the fractional excitations in a quantum paramagnetic state above the transition temperature as a proximity effect of the QSL phase.

In particular, unconventional excitations were observed by polarized Raman scattering in α -RuCl₃ (ref. 4). In this material,

Néel ordering sets in only at $T_c \sim 14$ K, whereas there is growing evidence^{15,22} that the Kitaev interaction is much larger than additional interactions such as the Heisenberg interaction, and hence finite-temperature signatures of the Kitaev QSL are expected to be observed in the paramagnetic state persisting in a broad temperature window above T_c .

The inset of Fig. 2 shows the integrated experimental Raman intensity for α -RuCl₃ as a function of temperature⁴. A background contribution, probably due to phonons, has been identified and subtracted⁴, as it persists up to very high T much larger than any magnetic scale. In this limit, it can be fitted to standard one-particle scattering which is proportional to $n + 1$, with $n = 1/(e^{\beta\omega} - 1)$ being the Bose distribution function ($\beta = 1/T$ is the inverse temperature and ω is the energy for bosons). The main panel (red symbols) shows the remaining, presumably dominantly magnetic contribution.

Most remarkably, the T dependence of the spectral weight up to high temperatures (more than an order of magnitude above T_c), does not follow the bosonic form expected for conventional insulating magnets in which both magnons and phonons obey Bose statistics. It is thus imperative to understand the origin of this anomalous contribution. This will provide a more direct test of the proximity to QSLs than an asymptotic low- T behaviour which is sensitive to the subdominant exchange interactions.

Results

The main panel of Fig. 2 provides a comparison of the T dependence of our theoretical results (blue circles) with the experimental data. The good agreement over a wide temperature range, from just above T_c up to a much higher scale ($\sim 15T_c$), offers compelling evidence that our Kitaev QSL theory correctly identifies the nature of fundamental excitations in the form of fractionalized fermions. This is further reinforced by noticing that the asymptotic two-fermion-scattering form $(1 - f)^2$, with $f = 1/(1 + e^{\beta\varepsilon})$ being the Fermi distribution function (ε is the energy for fermions), is a good fit of the response. In the following, we outline our calculations and explain how the two-fermion-scattering T -dependence emerges as a result of fractionalization.

We investigate the Raman spectrum at finite T for the Kitaev model using quantum Monte Carlo (QMC) simulations which enable the numerically exact calculation. This directly utilizes the fractionalization of quantum spins into two species of Majorana fermions: itinerant ‘matter’ and localized ‘flux’ fermions (see Methods for details). Crucially, the Raman response is elicited only by the itinerant Majorana fermions⁷, which allows us to detect their Fermi statistics more directly than in other dynamical responses⁶. Below we focus on the case of isotropic exchange couplings,

¹Department of Physics, Tokyo Institute of Technology, Meguro, Tokyo 152-8551, Japan. ²Department of Physics, Cavendish Laboratory, JJ Thomson Avenue, Cambridge CB3 0HE, UK. ³NRC Kurchatov Institute, 1 Kurchatov Square, Moscow 123182, Russia. ⁴Department of Applied Physics, University of Tokyo, Bunkyo, Tokyo 113-8656, Japan. ⁵Max Planck Institute for the Physics of Complex Systems, D-01187 Dresden, Germany.

*e-mail: nasu@phys.titech.ac.jp; jk628@cam.ac.uk

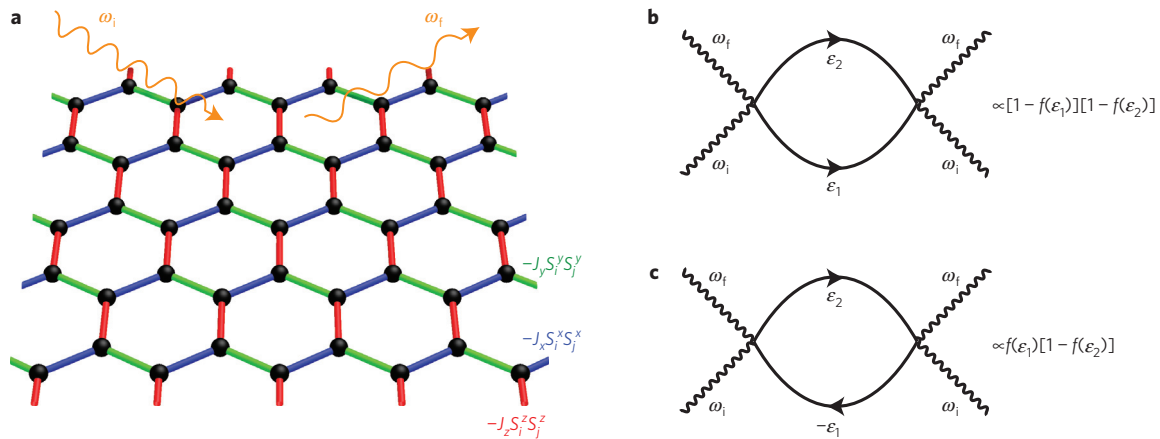


Figure 1 | Schematic pictures for the Kitaev model and Raman processes. **a**, Honeycomb lattice structure. Blue, green and red bonds represent Ising-like interactions between x -, y - and z -components of the $S = 1/2$ spins, respectively. Incoming and outgoing photons, whose frequencies are ω_i and ω_f , are also depicted. **b, c**, Feynman diagrams of the Raman scattering processes that correspond to a creation or annihilation of a pair of matter fermions (process (A)) (**b**) and a combination of creation and annihilation of the matter fermions (process (B)) (**c**). In process (A), a photon scattering creates two fermions with energies ε_1 and ε_2 , hence the Raman shift $\omega = \omega_f - \omega_i$ is equal to $\varepsilon_1 + \varepsilon_2$. In process (B), the scattering creates a fermion with energy ε_2 and annihilates a fermion with ε_1 simultaneously, hence, ω is equal to $\varepsilon_2 - \varepsilon_1$.

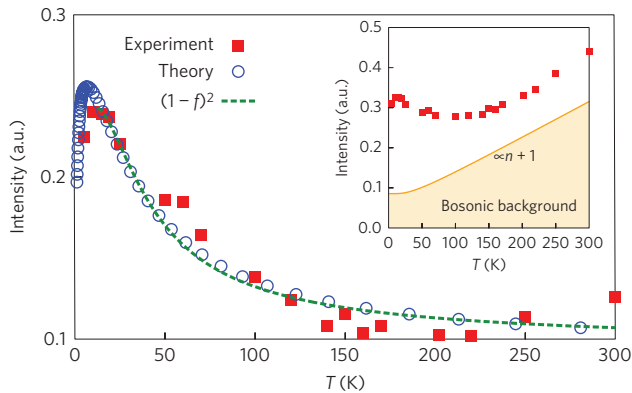


Figure 2 | Comparison between the numerical results and the experimental data for α -RuCl₃. Main panel: blue circles represent QMC data for a $L = 20$ cluster for the integrated Raman intensity I_{mid} shown in Fig. 3c. The errors evaluated by the standard deviation of the MC samplings are sufficiently smaller than the symbol size. Red squares are the experimental data in the energy window from 5 to 12.5 meV (ref. 4), from which the non-magnetic background is subtracted (see text). Green dashed lines represent the fitting by $a_M[1 - f(\varepsilon_M^*)]^2 + b_M$ (see caption of Fig. 3). We take $J = 10$ meV in calculating I_{mid} . Inset: red squares show the experimental raw data and the orange curve indicates the bosonic background. Note that the assignment of the bosonic background is slightly different from that in ref. 4. Details of the fitting procedure are given in Methods.

$J_x = J_y = J_z = J$; a small anisotropy plausible in real materials does not alter our main conclusions (see Supplementary Information). The thermodynamic behaviour exhibits two characteristic crossover T -scales originating from fractionalization at $T^*/J \sim 0.012$ and $T^{**}/J \sim 0.38$: the former is related to the condensation of flux Majorana fermions, set by the flux gap $\sim 0.06J$ (ref. 2), whereas the latter arises from the formation of matter Majorana fermions at much higher T , set by their bandwidth $\sim 1.5J$.

Figure 3a shows the QMC data for the Raman spectrum $I(\omega)$ at several T . At $T = 0$, it exhibits ω -linear behaviour in the low-energy region, due to a linear Dirac dispersion of matter Majorana fermions⁷. With increasing T above T^* , the low-energy part increases and the $\omega = 0$ contribution becomes nonzero, as shown in the figure for $T/J = 0.0375$. At higher T , the broad peak

in the intermediate energy range at $\omega/J \sim 1$ is suppressed above $T \sim T^{**}$. Indeed, the Raman spectrum at $T/J = 0.75$ shows no substantial energy dependence for $0 < \omega/J \lesssim 2$, as shown in Fig. 3a. For higher T , the intermediate-to-high-energy weight gradually decreases. The T and ω dependence of the Raman spectrum is summarized in Fig. 3b. The result clearly shows that the broad peak structure is slightly shifted to the low-energy side above T^* and the spectrum becomes featureless above T^{**} .

For further understanding of the T dependence of the Raman spectra, it is helpful to work in a basis of complex matter fermions constructed as a superposition of real Majorana fermions (see Methods). These elementary excitations determine the T -dependence because their occupation (in a fixed background of fluxes) is given by the Fermi distribution function. In detail, one needs to analyse two different processes contributing to Raman scattering²³: one consists of creation or annihilation of a pair of fermions (process (A)), with the other a combination of the creation of one fermion and the annihilation of another (process (B)) (see Methods for details). Process (A) is proportional to $[1 - f(\varepsilon_1)][1 - f(\varepsilon_2)]\delta(\omega - \varepsilon_1 - \varepsilon_2)$, where ω is the Raman shift, and ε_1 and ε_2 are the energies of fermions (see Fig. 1b). Process (B) is proportional to $f(\varepsilon_1)[1 - f(\varepsilon_2)]\delta(\omega + \varepsilon_1 - \varepsilon_2)$ and vanishes at $T = 0$ due to the absence of matter fermions in the ground state (see Fig. 1c). Because of their different frequency dependence—for example, (A) vanishes for $\omega \rightarrow 0$ at low T —their distinct T -behaviour can be extracted by looking at different frequency windows.

Figure 3c shows the T dependence of the integrated spectral weight in the intermediate energy window, I_{mid} for $0.5 < \omega/J < 1.25$ (see the hatched region in Fig. 3a). The same is used in Fig. 2 in accordance with the frequency window for the experimental data with $J = 10$ meV. We emphasize that the value of J is consistent not only with the spectral width and peak position of the Raman continuum at the lowest T (ref. 4), but also with the inelastic neutron scattering in α -RuCl₃ (ref. 15). As shown in Fig. 3c, I_{mid} has a non-monotonic change as a function of T : it grows above T^* with increasing T , but turns over to decrease above $T/J \sim 0.1$, yielding the shift of the peak structure in $I(\omega)$ to the low-energy side shown in Fig. 3b. Note that the decrease persists up to temperatures much higher than J due to thermal fluctuations of the itinerant Majorana fermions. We also highlight the contributions from the processes (A) and (B) in Fig. 3c. The result clearly indicates that I_{mid}

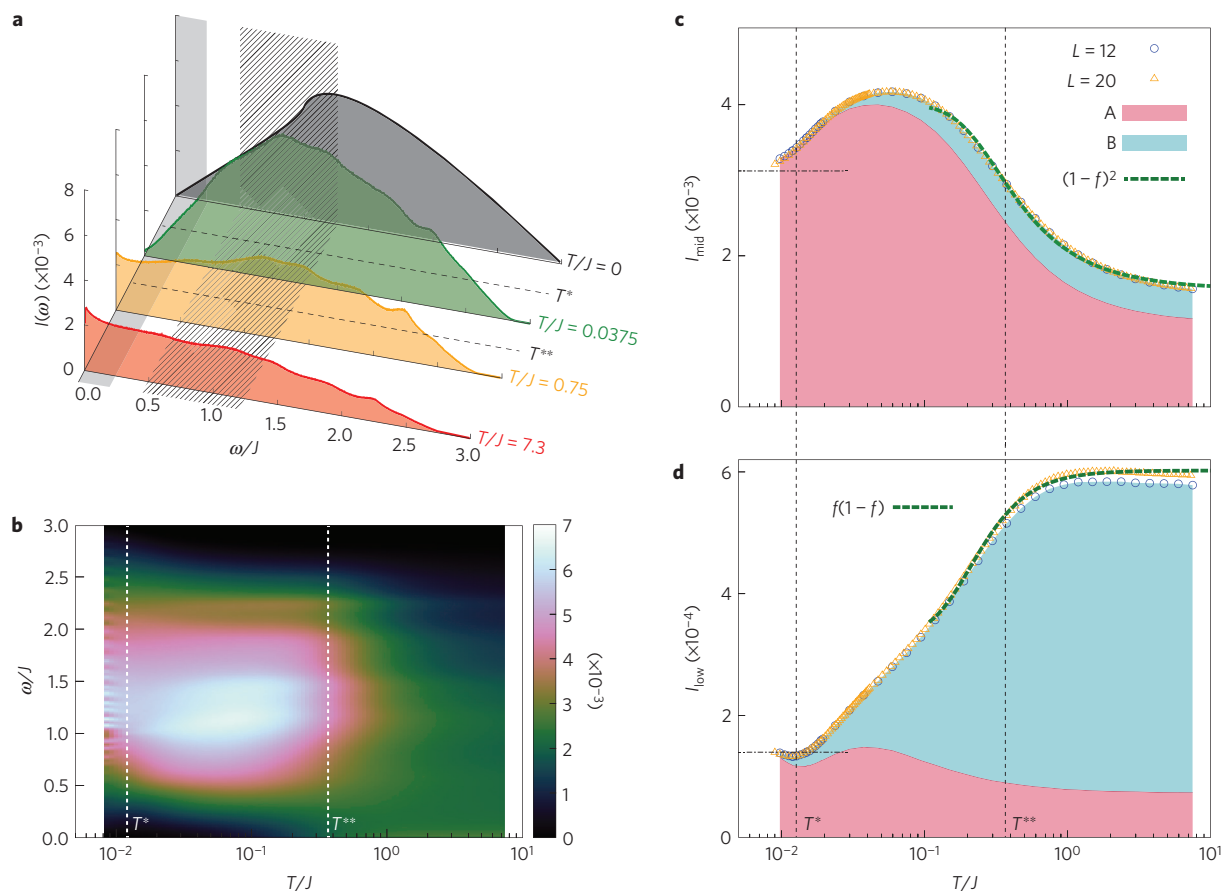


Figure 3 | Calculated Raman intensity for finite temperatures. **a**, ω dependences of the Raman spectra $I(\omega)$ at several T . **b**, Contour map of the Raman spectrum $I(\omega)$ in the T - ω plane. **c,d**, Integrated spectral weights I_{mid} for $0.5 < \omega/J < 1.25$ (**c**) and I_{low} for $0.0 < \omega/J < 0.25$ (**d**), whose energy ranges are indicated by the hatched and shaded areas in Fig. 3a, respectively. Green dashed lines represent fits using $a_M[1 - f(\varepsilon_M^*)]^2 + b_M$ with $\varepsilon_M^*/J = 0.58$ in **c**, and $a_L f(\varepsilon_L^*)[1 - f(\varepsilon_L^*)] + b_L$ with $\varepsilon_L^*/J = 0.42$ in **d** (see Supplementary Information). Here, $f(\varepsilon) = (1 + e^{\beta\varepsilon})^{-1}$ is the Fermi distribution function with zero chemical potential. Horizontal dashed-dotted lines represent the values of I_{low} and I_{mid} at $T = 0$ (refs 7,23). The red and blue areas in **c** and **d** highlight the contributions to the integrated Raman intensities from the processes (A) and (B), respectively. The errors evaluated by the standard deviation of the MC samplings are sufficiently smaller than the symbol size. Vertical dotted lines indicate two crossover temperatures, T^* and T^{**} .

is dominated by the process (A), which supports the scaling with $(1 - f)^2$ (see Supplementary Information).

Meanwhile, the results presented in Fig. 3d covering the low-energy window, I_{low} for $0.0 < \omega/J < 0.25$ (see the shaded region in Fig. 3a), have a different T -dependence. The increase around T^* is because the Dirac semimetallic dip in the itinerant fermion system is filled in due to thermal fluctuations of the flux fermions⁹. Moreover, with increasing T , I_{low} saturates around the high- T crossover T^{**} . As shown in Fig. 3d, above $T/J \sim 0.1$, I_{low} is dominated by the process (B), indicating that the T dependence is well fitted by $f(1 - f)$. However, the intensity I_{low} is one order of magnitude smaller than I_{mid} .

Discussion

The striking T dependence of the Raman intensity observed in experiments can be naturally attributed to the response from fractionalized fermionic Majorana excitations, dominantly from pairs of creation and annihilation of matter fermions. The T dependence is qualitatively different from that of conventional insulating magnets which show bosonic Raman spectra from two-magnon scattering²⁴. It is important to note that here we are dealing with a two-dimensional magnet^{13–15}. In one dimension, there is no such crisp distinction between Bose and Fermi statistics, as in the absence of true exchange processes, bosons with hardcore repulsion

are rather similar to fermions obeying the Pauli principle; and on the other hand the roles of topology and order in two dimensions are quite distinct from a one-dimensional case²⁵.

We note that the behaviour below and around T_c is non-universal, as indicated by the strong sample dependence of T_c (ref. 13,15). All features connected to the long-range ordering quickly disappear above T_c , and the universal aspect related with the dominant Kitaev interaction appears in a wide T range. In fact, a recent exact diagonalization study presents evidence of fractional excitations above T_c (ref. 26).

The crucial observation here is that the unexpected fermionic contribution is clearly observed over a remarkably wide T range, more than an order of magnitude higher than the transition temperature into the incidental low-temperature Néel order. This approach is distinct from the conventional quest for exotic properties of QSLs, where the experimental hallmark of fermionic excitations has mainly been pursued in asymptotic T behaviour—for example, in the T -linear specific heat for temperatures much lower than the interaction energy. However, the low- T analyses of such thermodynamic quantities are further complicated by the need to distinguish between QSLs, glassy behaviour, spurious order, and other low-energy contributions typified, for example, by nuclear spins. Our finding provides a direct way of identifying QSL behaviour, and in particular, the presence of fermionic excitations.

This, we hope, will stimulate further studies of other dynamical quantities in the wide T range¹⁵ as well as studies of other candidate materials such as $A_2\text{IrO}_3$ ($A = \text{Li}, \text{Na}$)²⁷.

Methods

Methods, including statements of data availability and any associated accession codes and references, are available in the [online version of this paper](#).

Received 16 February 2016; accepted 19 May 2016;
published online 4 July 2016

References

- Anderson, P. W. Resonating valence bonds: a new kind of insulator? *Mater. Res. Bull.* **8**, 153–160 (1973).
- Kitaev, A. Anyons in an exactly solved model and beyond. *Ann. Phys.* **321**, 2–111 (2006).
- Lacroix, C., Mendels, P. & Mila, F. *Introduction to Frustrated Magnetism* (Springer Series in Solid-State Sciences, Springer, 2011).
- Sandilands, L. J., Tian, Y., Plumb, K. W., Kim, Y.-J. & Burch, K. S. Scattering continuum and possible fractionalized excitations in $\alpha\text{-RuCl}_3$. *Phys. Rev. Lett.* **114**, 147201 (2015).
- Baskaran, G., Mandal, S. & Shankar, R. Exact results for spin dynamics and fractionalization in the Kitaev model. *Phys. Rev. Lett.* **98**, 247201 (2007).
- Knolle, J., Kovrizhin, D. L., Chalker, J. T. & Moessner, R. Dynamics of a two-dimensional quantum spin liquid: signatures of emergent Majorana fermions and fluxes. *Phys. Rev. Lett.* **112**, 207203 (2014).
- Knolle, J., Chern, G.-W., Kovrizhin, D. L., Moessner, R. & Perkins, N. B. Raman scattering signatures of Kitaev spin liquids in $A_2\text{IrO}_3$ iridates with $A = \text{Na}$ or Li . *Phys. Rev. Lett.* **113**, 187201 (2014).
- Nasu, J., Udagawa, M. & Motome, Y. Vaporization of Kitaev spin liquids. *Phys. Rev. Lett.* **113**, 197205 (2014).
- Nasu, J., Udagawa, M. & Motome, Y. Thermal fractionalization of quantum spins in a Kitaev model: temperature-linear specific heat and coherent transport of Majorana fermions. *Phys. Rev. B* **92**, 115122 (2015).
- Jackeli, G. & Khaliullin, G. Mott insulators in the strong spin-orbit coupling limit: from Heisenberg to a quantum compass and Kitaev models. *Phys. Rev. Lett.* **102**, 017205 (2009).
- Singh, Y. *et al.* Relevance of the Heisenberg–Kitaev model for the honeycomb lattice iridates $A_2\text{IrO}_3$. *Phys. Rev. Lett.* **108**, 127203 (2012).
- Comin, R. *et al.* Na_2IrO_3 as a novel relativistic Mott insulator with a 340-meV gap. *Phys. Rev. Lett.* **109**, 266406 (2012).
- Kubota, Y., Tanaka, H., Ono, T., Narumi, Y. & Kindo, K. Successive magnetic phase transitions in $\alpha\text{-RuCl}_3$: XY-like frustrated magnet on the honeycomb lattice. *Phys. Rev. B* **91**, 094422 (2015).
- Plumb, K. W. *et al.* $\alpha\text{-RuCl}_3$: a spin-orbit assisted Mott insulator on a honeycomb lattice. *Phys. Rev. B* **90**, 041112 (2014).
- Banerjee, A. *et al.* Proximate Kitaev quantum spin liquid behaviour in a honeycomb magnet. *Nature Mater.* doi:10.1038/nmat4604 (2016).
- Chaloupka, J., Jackeli, G. & Khaliullin, G. Kitaev–Heisenberg model on a honeycomb lattice: possible exotic phases in iridium oxides $A_2\text{IrO}_3$. *Phys. Rev. Lett.* **105**, 027204 (2010).
- Reuther, J., Thomale, R. & Trebst, S. Finite-temperature phase diagram of the Heisenberg–Kitaev model. *Phys. Rev. B* **84**, 100406 (2011).
- Chaloupka, J., Jackeli, G. & Khaliullin, G. Zigzag magnetic order in the iridium oxide Na_2IrO_3 . *Phys. Rev. Lett.* **110**, 097204 (2013).
- Yamaji, Y., Nomura, Y., Kurita, M., Arita, R. & Imada, M. First-principles study of the honeycomb-lattice iridates Na_2IrO_3 in the presence of strong spin-orbit interaction and electron correlations. *Phys. Rev. Lett.* **113**, 107201 (2014).
- Katukuri, V. M. *et al.* Kitaev interactions between $j = 1/2$ moments in honeycomb Na_2IrO_3 are large and ferromagnetic: insights from *ab initio* quantum chemistry calculations. *New J. Phys.* **16**, 013056 (2014).
- Foyevtsova, K., Jeschke, H. O., Mazin, I. I., Khomskii, D. I. & Valentí, R. *Ab initio* analysis of the tight-binding parameters and magnetic interactions in Na_2IrO_3 . *Phys. Rev. B* **88**, 035107 (2013).
- Kim, H.-S., Shankar, V. V., Catuneanu, A. & Kee, H.-Y. Kitaev magnetism in honeycomb RuCl_3 with intermediate spin-orbit coupling. *Phys. Rev. B* **91**, 241110 (2015).
- Perreault, B., Knolle, J., Perkins, N. B. & Burnell, F. J. Theory of Raman response in three-dimensional Kitaev spin liquids: application to β - and $\gamma\text{-Li}_2\text{IrO}_3$ compounds. *Phys. Rev. B* **92**, 094439 (2015).
- Sandvik, A. W., Capponi, S., Poilblanc, D. & Dagotto, E. Numerical calculations of the B_{1g} Raman spectrum of the two-dimensional Heisenberg model. *Phys. Rev. B* **57**, 8478–8493 (1998).
- Wen, X.-G. *Quantum Field Theory of Many-body Systems: From the Origin of Sound to an Origin of Light and Electrons* Ch. 8 & 9 (Oxford Univ. Press, 2007).
- Yamaji, Y. *et al.* Clues and criteria for designing Kitaev spin liquid revealed by thermal and spin excitations of honeycomb iridates Na_2IrO_3 . *Phys. Rev. B* **93**, 174425 (2016).
- Gretarsson, H. *et al.* Magnetic excitation spectrum of Na_2IrO_3 probed with resonant inelastic X-ray scattering. *Phys. Rev. B* **87**, 220407 (2013).

Acknowledgements

We thank M. Udagawa, K. Burch, P. Lemmens, B. Perreault, F. N. Burnell, N. B. Perkins, S. Kourtis, K. Ohgushi and J. Yoshitake for fruitful discussions. J.K., D.L.K. and R.M. are very grateful to J. T. Chalker for collaborations on related work. We are especially grateful to L. Sandilands and K. Burch for sending us their experimental data on $\alpha\text{-RuCl}_3$. This work is supported by Grant-in-Aid for Scientific Research under Grant No. 24340076, 15K13533, 16H00987, and 16H02206, the Strategic Programs for Innovative Research (SPIRE), MEXT, the Computational Materials Science Initiative (CMSI), Japan, and the DFG via SFB 1143. The work of J.K. is supported by a Fellowship within the Postdoc-Program of the German Academic Exchange Service (DAAD). D.L.K. is supported by EPSRC Grant No. EP/M007928/1. Parts of the numerical calculations are performed in the supercomputing systems in ISSP, the University of Tokyo.

Author contributions

All authors contributed to conception, execution and write-up of this project. The numerical simulations were performed by J.N.

Additional information

Supplementary information is available in the [online version of the paper](#). Reprints and permissions information is available online at www.nature.com/reprints. Correspondence and requests for materials should be addressed to J.N. or J.K.

Competing financial interests

The authors declare no competing financial interests.

Methods

Monte Carlo simulation. The Hamiltonian of the Kitaev model on the honeycomb lattice is given by

$$\mathcal{H} = -J_x \sum_{\langle jk \rangle_x} S_j^x S_k^x - J_y \sum_{\langle jk \rangle_y} S_j^y S_k^y - J_z \sum_{\langle jk \rangle_z} S_j^z S_k^z \quad (1)$$

where $S_j = (S_j^x, S_j^y, S_j^z)$ represents an $S=1/2$ spin on site j , and $\langle jk \rangle_\gamma$ stands for a nearest-neighbour $\gamma (=x, y, z)$ bond shown in Fig. 1a². By using the Jordan–Wigner transformation and introducing two kinds of Majorana fermions, c_j and \tilde{c}_j ^{28,29}, the model is rewritten as

$$\mathcal{H} = \frac{iJ_x}{4} \sum_{\langle jk \rangle_x} c_j c_k - \frac{iJ_y}{4} \sum_{\langle jk \rangle_y} c_j c_k - \frac{iJ_z}{4} \sum_{\langle jk \rangle_z} \eta_r c_j c_k \quad (2)$$

where $\langle jk \rangle_\gamma$ is the nearest-neighbour pair satisfying $j < k$ on the γ bond, and $\eta_r = i\tilde{c}_j c_k$ is a Z_2 variable defined on the z bond (r is the label for the bond), which takes ± 1 . Equation (2) describes free itinerant Majorana fermions coupled to classical Z_2 variables $\{\eta_r\}$. Although the configurations of $\{\eta_r\}$ are thermally disturbed away from the ground state configuration with all $\eta_r = 1$, the thermodynamic behaviour can be obtained by properly sampling $\{\eta_r\}$ as follows. As the Hamiltonian for a given configuration of $\{\eta_r\}$ is bilinear in terms of c operators, it is easily diagonalized as

$$\mathcal{H}(\{\eta_r\}) = \sum_\lambda \varepsilon_\lambda \left(f_\lambda^\dagger f_\lambda - \frac{1}{2} \right) \quad (3)$$

Here, we introduce complex matter fermions f_λ with the eigenenergies $\varepsilon_\lambda (\geq 0)$, which are related to c by

$$c_j = \sum_\lambda \left(X_{j\lambda} f_\lambda + X_{j\lambda}^* f_\lambda^\dagger \right) \quad (4)$$

where $X_{j\lambda}$ is introduced so as to diagonalize the Hamiltonian. Then, we evaluate the free energy $F_f(\{\eta_r\}) = -\beta^{-1} \ln Z_f(\{\eta_r\})$ for the configuration $\{\eta_r\}$, where $Z_f(\{\eta_r\}) = \text{Tr}_{\{c\}} e^{-\beta \mathcal{H}(\{\eta_r\})}$; $\beta = 1/T$ is the inverse temperature, and we set $k_B = 1$. The thermal average of an operator \mathcal{O} is given by

$$\langle \mathcal{O} \rangle = \frac{1}{Z} \sum_{\{\eta_r\}} \text{Tr}_{\{c\}} [\mathcal{O} e^{-\beta \mathcal{H}}] = \langle \bar{\mathcal{O}}(\{\eta_r\}) \rangle_\eta \quad (5)$$

where we define $\bar{\mathcal{O}}(\{\eta_r\}) = Z_f(\{\eta_r\})^{-1} \text{Tr}_{\{c\}} [\mathcal{O} e^{-\beta \mathcal{H}(\{\eta_r\})}]$ and $\langle \cdots \rangle_\eta = Z^{-1} \sum_{\{\eta_r\}} [\cdots] e^{-\beta F_f(\{\eta_r\})}$, with Z being the partition function of the system. In our calculations, we take the sum over configurations $\{\eta_r\}$ in the average $\langle \cdots \rangle_\eta$ by performing Monte Carlo (MC) simulations so as to reproduce the distribution $e^{-\beta F_f(\{\eta_r\})}$. This admits the quantum MC (QMC) simulation which is free from the sign problem⁹.

Raman spectrum. To calculate the Raman spectrum at finite T , we employ the Loudon–Fleury (L–F) approach^{30,31} by following previous $T=0$ studies^{7,23}: the LF operator for the Kitaev model is given by $\mathcal{R} = \sum_{\gamma=x,y,z} \sum_{\langle jk \rangle_\gamma} (\epsilon_{\text{in}} \cdot d^\gamma) (\epsilon_{\text{out}} \cdot d^\gamma) J^\gamma S_j^\gamma S_k^\gamma$, where ϵ_{in} and ϵ_{out} are the polarization vectors of the incoming and outgoing photons and d^γ is the vector connecting sites on a NN γ bond. Using the LF operator, the Raman intensity is given by $I^{\text{LF}}(\omega) = 1/N \int_{-\infty}^{\infty} dt e^{i\omega t} \langle \mathcal{R}(t) \mathcal{R}(0) \rangle$, where $\mathcal{R}(t) = e^{i\mathcal{H}t} \mathcal{R} e^{-i\mathcal{H}t}$ and N is the number of sites; l and l' denote the directions of ϵ_{in} and ϵ_{out} in \mathcal{R} , respectively. Note that the following relation is satisfied in the isotropic case⁷:

$$I^{\text{xx}}(\omega) = I^{\text{yy}}(\omega) = I^{\text{zz}}(\omega) \equiv I(\omega) \quad (6)$$

In terms of the Majorana fermions, the LF operator is described by a bilinear form of c operators as

$$\mathcal{R} = \frac{1}{2} \sum_{jk} B_{jk}(\{\eta_r\}) c_j c_k \quad (7)$$

where $B(\{\eta_r\})$ is a Hermitian matrix with pure imaginary elements. Note that $\mathcal{R}(t)$ is simply given by $1/2 \sum_{jk} B_{jk}(\{\eta_r\}) c_j(t) c_k(t)$ as all $\{\eta_r\}$ commute with the Hamiltonian. It is this property which allows us to evaluate exactly the dynamical correlator of \mathcal{R} . Using equation (4), we obtain

$$\mathcal{R} = \frac{1}{2} \sum_{\lambda\lambda'} [C_{\lambda\lambda'} (2f_\lambda^\dagger f_{\lambda'} - \delta_{\lambda\lambda'}) + D_{\lambda\lambda'} f_\lambda^\dagger f_{\lambda'}^\dagger + D_{\lambda\lambda'}^* f_\lambda f_{\lambda'}] \quad (8)$$

where $C_{\lambda\lambda'} = \sum_{jk} B_{jk} X_{j\lambda}^* X_{k\lambda'}$ and $D_{\lambda\lambda'} = \sum_{jk} B_{jk} X_{j\lambda}^* X_{k\lambda'}^*$. By applying Wick's theorem, we obtain the Raman intensity for a given configuration $\{\eta_r\}$ as

$$\begin{aligned} \bar{I}^{\text{LF}}(\omega; \{\eta_r\}) = & \frac{1}{N} \sum_{\lambda\lambda'} [2\pi |C_{\lambda\lambda'}|^2 f(\varepsilon_\lambda) [1 - f(\varepsilon_{\lambda'})] \delta(\omega + \varepsilon_\lambda - \varepsilon_{\lambda'}) \\ & + \pi |D_{\lambda\lambda'}|^2 [1 - f(\varepsilon_\lambda)] [1 - f(\varepsilon_{\lambda'})] \delta(\omega - \varepsilon_\lambda - \varepsilon_{\lambda'})] \end{aligned} \quad (9)$$

where $\omega > 0$. Finally, the thermal average is evaluated as $I^{\text{LF}}(\omega) = \langle \bar{I}^{\text{LF}}(\omega; \{\eta_r\}) \rangle_\eta$ using the QMC simulation.

The terms in equation (9) describe two different Raman processes, which show different T dependences via the Fermi distribution function $f(\varepsilon)$: the first term corresponds to the process (B) (Fig. 1c) and the second term corresponds to the process (A) (Fig. 1b). Thus, the T dependence of the Raman intensity provides a good indicator of fermionic excitations in Kitaev QSLs.

Following our previous QMC study⁹, we have performed more than 30,000 MC steps for the measurements after 10,000 MC steps for the thermalization using parallel tempering technique, for $N = 2L^2$ clusters with $L = 12$ and 20. The Raman intensity $I^{\text{LF}}(\omega)$ is computed from 3,000 samples during the 30,000 MC steps. The statistical errors are evaluated by the corresponding standard deviation. However, it turns out that the errors are sufficiently smaller than the symbol sizes in the plots in Figs 2, 3c, and 3d, and hence, are not shown.

Details of the fitting to experimental results. We define the Raman spectrum of the Kitaev model with $J = J_x = J_y = J_z$ as $I_K(\omega, J)$, which is $I(\omega)$ in equation (6) calculated by QMC for the $L = 20$ cluster. The bosonic background is taken to be proportional to $I_B(\omega) \equiv n(\omega) + 1 = e^{\beta\omega} / (e^{\beta\omega} - 1)$, as in ref. 4. Then, we assume that the total spectral weight $I_{\text{total}}(\omega, J)$ is given by

$$I_{\text{total}}(\omega; J, \alpha_K, \alpha_B) = \alpha_K I_K(\omega, J) + \alpha_B I_B(\omega) \quad (10)$$

where α_K and α_B are the coefficients to be determined in the fitting procedure below. The integrated intensity for the intermediate energy window $0.5 < \omega/J < 1.25$ is also introduced as

$$I_{\text{total}}^{\text{mid}}(J, \alpha_K, \alpha_B) = \int_{0.5}^{1.25} I_{\text{total}}(\omega; J, \alpha_K, \alpha_B) d\omega = \alpha_K I_K^{\text{mid}}(J) + \alpha_B I_B^{\text{mid}}(J) \quad (11)$$

where $I_K^{\text{mid}}(J)$ is equivalent to I_{mid} in the main text. On the other hand, the experimental data for the integrated intensity within the same energy window is obtained by

$$I_{\text{exp}}(J) = \int_{0.5}^{1.25} I_{\text{exp}}(\omega) d\omega \quad (12)$$

where $I_{\text{exp}}(\omega)$ is the E_g component of the Raman spectrum measured for α -RuCl₃ (ref. 4). In Fig. 2, we assume $J = 10$ meV and determine the coefficients α_K and α_B so as to fit $I_{\text{total}}^{\text{mid}}(J, \alpha_K, \alpha_B)$ to $I_{\text{exp}}(J)$ in the energy window from 5 to 12.5 meV (see Supplementary Information for the choice of J); we compute $I_{\text{exp}}(J)$ from the experimental data provided by the authors of ref. 4. We denote the optimized coefficients by α_K^* and α_B^* . In the main panel of this figure, the red squares and blue circles represent $I_{\text{exp}}(J) - \alpha_B^* I_B(J)$ and $\alpha_K^* I_K(J)$, respectively. In the inset, the red squares represent $I_{\text{exp}}(J)$ and the orange line represents $\alpha_B^* I_B(J)$.

Data availability. Experimental Raman spectroscopy data were originally reported in ref. 4. All other data that support the plots within this paper and other findings of this study are available from the corresponding authors upon request.

References

- Chen, H.-D. & Hu, J. Exact mapping between classical and topological orders in two-dimensional spin systems. *Phys. Rev. B* **76**, 193101 (2007).
- Feng, X.-Y., Zhang, G.-M. & Xiang, T. Topological characterization of quantum phase transitions in a spin-1/2 model. *Phys. Rev. Lett.* **98**, 087204 (2007).
- Fleury, P. A. & Loudon, R. Scattering of light by one- and two-magnon excitations. *Phys. Rev.* **166**, 514–530 (1968).
- Shastry, B. S. & Shraiman, B. I. Theory of Raman scattering in Mott–Hubbard systems. *Phys. Rev. Lett.* **65**, 1068–1071 (1990).